ADVANCED MATERIALS INTERFACES
www.advmatinterfaces.de

In Situ Growth of Fe_2O_3 Nanoparticles on Highly Porous Graphene/Polyimide-Based Carbon Aerogel Nanocomposites for Effectively Selective Detection of Dopamine

Youfang Zhang, Wei Gao, Lizeng Zuo, Longsheng Zhang, Yunpeng Huang, Hengyi Lu, Wei Fan, and Tianxi Liu**

It is very important to develop a simple, efficient, and scaleable method for detection of dopamine (DA) with high sensitivity and selectivity to diagnose some serious neurological diseases. Herein, electro-catalysts for detection of DA are simply prepared based on Fe_2O_3 nanoparticles (NPs) decorated on highly porous carbon aerogels (CAs), which are derived from KOH activated graphene-polyimide aerogels. In the hierarchical nanocomposites (NCs), CAs provide large specific surface area, abundant mesopores, and macropores, and many sites for in situ growth of Fe_2O_3 NPs, thus effectively preventing the aggregation of Fe_2O_3 NPs. Moreover, CAs with 3D interconnected porous structures are able to shorten the charge transfer pathways through the intimate interaction between CAs and Fe_2O_3 NPs. Therefore, when applied as electro-catalysts for detection of DA, the optimized NC exhibits rapid amperometric response and a low detection limit of 0.109×10^{-6} M (S/N = 3), with a wide linear concentration range from 5 to 500×10^{-6} M. In addition, the oxidation peak of DA can be readily distinguished from the interference of uric acid and ascorbic acid. Therefore, the highly porous CAs derived from KOH activated graphene-polyimide aerogels are excellent substrates for in situ growth of Fe_2O_3 NPs, exhibiting high electrocatalytic activity for DA detection.

1. Introduction

Dopamine (DA) is a vital monoamine neurotransmitter that plays important roles in the activities of the central nervous, renal, hormonal, and cardiovascular system.[1] The level of DA in mammalian body seriously affects the emotion (such as depression, excitement) of mammals. The concentration exception of DA may result in neurological diseases, such as Parkinson's disease, Huntington's disease, schizophrenia, Alzheimer's disease, drug addiction, and so on.[2,3] Therefore, the detection of DA has attracted much attention and more and more methods have been exploited for DA detection, such as capillary electrophoresis, fluorescence quenching method, liquid chromatography, gas chromatography, and mass spectrometry.[4,5] Although these methods are effective for the detection of DA, most of them require expensive equipment and are limited by low-sensitivity, bad selectivity, high-cost, and time-consuming process. Thus, it is urgent to develop simple and viable approaches for the detection of DA. Electrochemical detection is proved to be an ideal method on account of its simple operation, real-time detection, low-cost, fast response, high sensitivity, and excellent selectivity.[6–12] However, the coexistence of uric acid (UA) and ascorbic acid (AA) could cause signal interference and greatly hinder the effectiveness of electrochemical detection of DA. Therefore, it is necessary to distinguish the overlapping oxidation and reduction signals from AA and UA, and improve the selectivity and sensitivity of DA detection.

Currently, researches on electrochemical sensors mainly focus on the development of high-efficiency electrocatalytic materials and small sized portable tester. Metal and metal oxide nanoparticles (NPs),[13–21] such as Pt, Pd, Ag, Au, Ni, Co_3O_4, and Fe_xO_y,[22–28] have been extensively investigated in recent years due to their high selectivity and sensitivity for detection of various vital materials. Among them, Fe_2O_3 stands out for its nontoxicity, biological and chemical inertness, excellent electrical and catalytic properties.[29–31] Thus, Fe_2O_3 NPs modified electrode can be widely applied as electrochemical sensors in non-enzymatic glucose,[32–34] uric acid,[35,36] H_2O_2,[37–39] choline,[40] ethanol,[41–43] nitric oxide,[44] H_2S,[45] nitrite,[46] and DA detection.[47] However, the electrochemical performance of

Y. F. Zhang, W. Gao, L. Z. Zuo, L. S. Zhang,
Y. P. Huang, H. Y. Lu, Prof. T. X. Liu
State Key Laboratory of Molecular Engineering of Polymers
Department of Macromolecular Science
Fudan University
Shanghai 200433, P. R. China
E-mail: txliu@fudan.edu.cn, txliu@dhu.edu.cn

Dr. W. Fan, Prof. T. X. Liu
State Key Laboratory of Modification of Chemical Fibers
and Polymer Materials
College of Materials Science and Engineering
Donghua University
Shanghai 201620, P. R. China
E-mail: weifan@dhu.edu.cn

DOI: 10.1002/admi.201600137

© 2016 WILEY-VCH Verlag GmbH & Co. KGaA, Weinheim

Fe_2O_3 NPs greatly suffers from their easy aggregation, poor dispersibility and conductivity. In this regard, preparation of uniformly distributed Fe_2O_3 NPs on a conductive substrate is an effective strategy to enhance their electrochemical activity for detection performance.

To solve this problem, many kinds of substrates, such as SnO_2,[48–51] polymer materials,[52–57] graphene,[58–63] carbon nanotubes,[64,65] carbon nanofibers,[17] have been widely developed. For example, Radhakrishnan et al.[46] reported that Fe_2O_3 NPs decorated on reduced graphene oxide (rGO) nanosheets exhibited excellent electrical coupling to the rGO nanosheets, resulting in excellent electrochemical detection for nitrite with a very low detection limit of 15×10^{-9} M. In another report, α-Fe_2O_3 nanosheets are hierarchically assembled onto the surface of SnO_2 hollow nanospheres, and the composite demonstrates superior sensing performance toward ethanol in comparison to a single component.[45]

Carbon aerogels (CAs) are a type of carbon materials with 3D porous nanostructures, which exhibit unique properties, such as high porosity, large surface area, high electrical conductivity, and chemical stability. As a consequence, CAs can serve as excellent substrates for the growth of metal or metal oxide NPs and promote electron transfer between the substrate and the active materials. In our previous work, we have successfully prepared graphene/polyimide (G-PI) based CA with hierarchical porous structures.[66] In this work, we further optimized the experiment condition and prepared KOH activated G-PI (a-G-PI) based CAs with much higher surface area, which were further employed as a 3D conductive substrates for in situ growth of nanosized Fe_2O_3 NPs. In this well-designed structure, highly porous CAs can form 3D inter-connected frameworks, which could not only prevent the aggregation of Fe_2O_3 NPs, but also favor ion diffusion and charge transport during the electrochemical process for DA detection. As a result, the optimized Fe_2O_3/a-G-PI based CA nanocomposite exhibits rapid amperometric response and a low detection limit of 0.109×10^{-6} M (S/N = 3), demonstrating superior sensing performance to that of pure Fe_2O_3 NPs in terms of DA detection. In addition, the oxidation peak of DA can be readily distinguished from the interference of uric acid and ascorbic acid. Therefore, this highly porous CAs supported Fe_2O_3 NPs modified electrode can be a promising sensor for DA detection.

2. Results and Discussion

2.1. Morphology and Structures of Fe_2O_3/a-G-PI Based CA NCs

The preparation process of a-G-PI based CA and Fe_2O_3/a-G-PI based CA NCs is shown in **Figure 1**. Fe_2O_3/a-G-PI based CA NCs with various Fe_2O_3 amount were prepared by an in situ solvothermal reaction method and the obtained samples were denoted as Fe_2O_3/a-G-PI based CA NCs-1, Fe_2O_3/a-G-PI based CA NCs-2 and Fe_2O_3/a-G-PI based CA NCs-5 according to the initial amount of ferric nitrate nonahydrate. First, the typical morphology of the synthesized pure PI based CA, a-PI based CA, and a-G-PI based CA are shown in **Figure 2**. As exhibited in Figure 2A,B, pure PI based CA has large pores with 1–5 µm in size, and the wall between the pores is solid. However, a great many of large and relatively uniform circular holes can be clearly observed from the overview image of a-PI based CAs and a-G-PI based CAs (Figure 2C–F), which can be attributed to the sublimation of small ice crystals during the freeze-drying process. Close observation of a-PI based CAs shows a lot of irregular pore structures, which originates from etching and carving of a flat carbon surface (inset image in Figure 2D). As is well known, KOH activation is an effective method to generate the porous network in carbon based materials. According to the classic mechanism for KOH activation,[67] the reaction of KOH and carbon with heating (400–800 °C) proceeds in the following five simultaneous/consecutive reactions

$$6KOH + 2C = 2K + 3H_2 + 2K_2CO_3 \tag{1}$$

$$K_2CO_3 = K_2O + CO_2 \tag{2}$$

$$CO_2 + C = 2CO \tag{3}$$

$$K_2CO_3 + 2C = 2K + 3CO \tag{4}$$

$$K_2O + C = 2K + CO \tag{5}$$

The first one is primary reaction, which starts with solid–solid reactions between KOH and carbon, producing a lot of hydrogen and K_2CO_3. Then, the as-formed K_2CO_3 can easily chemically decompose into K_2O and CO_2 with heat. In addition, the intermediate K_2CO_3 can also react with carbon and generate metallic potassium (K) and CO gas. Consecutively, CO_2 can be reduced by carbon to CO and K_2O can be reduced into K at high temperature. In brief, the process of KOH activation consists of both chemical activation and physical activation. Based on the oxidation–reduction reactions between potassium compounds and carbon element or carbon compounds, the carbon framework is etched into porous network and this consumption process of carbon is named as the chemical activation. As for the physical activation, there are two manifestation modes. Firstly, the formation of gas like H_2, CO, CO_2 in the chemical activation process can help generate the pores. Secondly, the metallic potassium and potassium compounds derived from the chemical activation could efficiently expand carbon lattices by intercalating into carbon lattices. After the removal of the metallic potassium and potassium compounds by subsequent washing, the expanded carbon framework is maintained without any collapses and the porous struncture is created. However, from close observation of a-G-PI based CAs (Figure 2F), the porous structure is different from that of a-PI based CAs. It can be clearly observed that there are a lot of regular circular pores with diameter of about 200 nm, which may be formed during the sol–gel process. In this process, adequate GO nanosheets strongly interact with PAA due to the aboundant oxygen-containing groups, like hydroxyl, carboxylic acid and epoxy groups on the surface of GO nanosheets. The increased crosslinking points generated from the strong interaction of GO nanosheets and PAA chains can result in smaller and uniform pores. Thus, hierarchical 3D networks are simply constructed by the crosslinking effect of graphene and KOH activation.

© 2016 WILEY-VCH Verlag GmbH & Co. KGaA, Weinheim

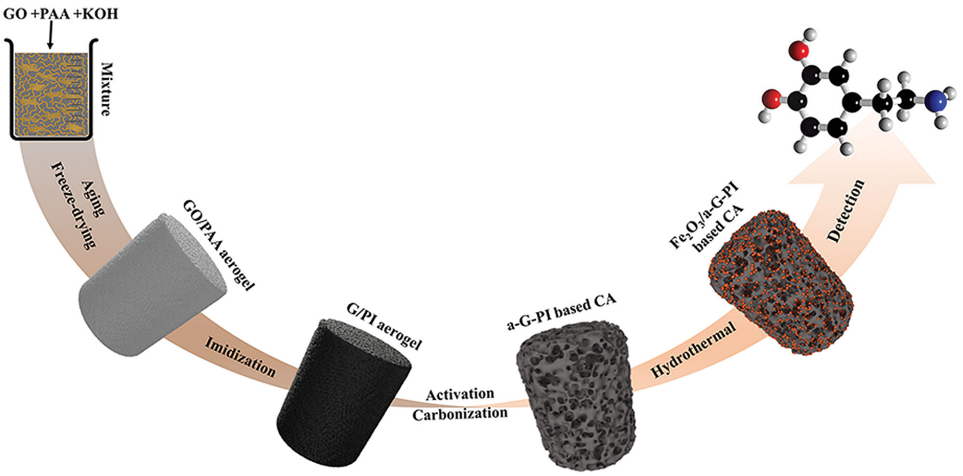

Figure 1. Schematic illustration of the preparation of Fe_2O_3/a-G-PI based CA NCs.

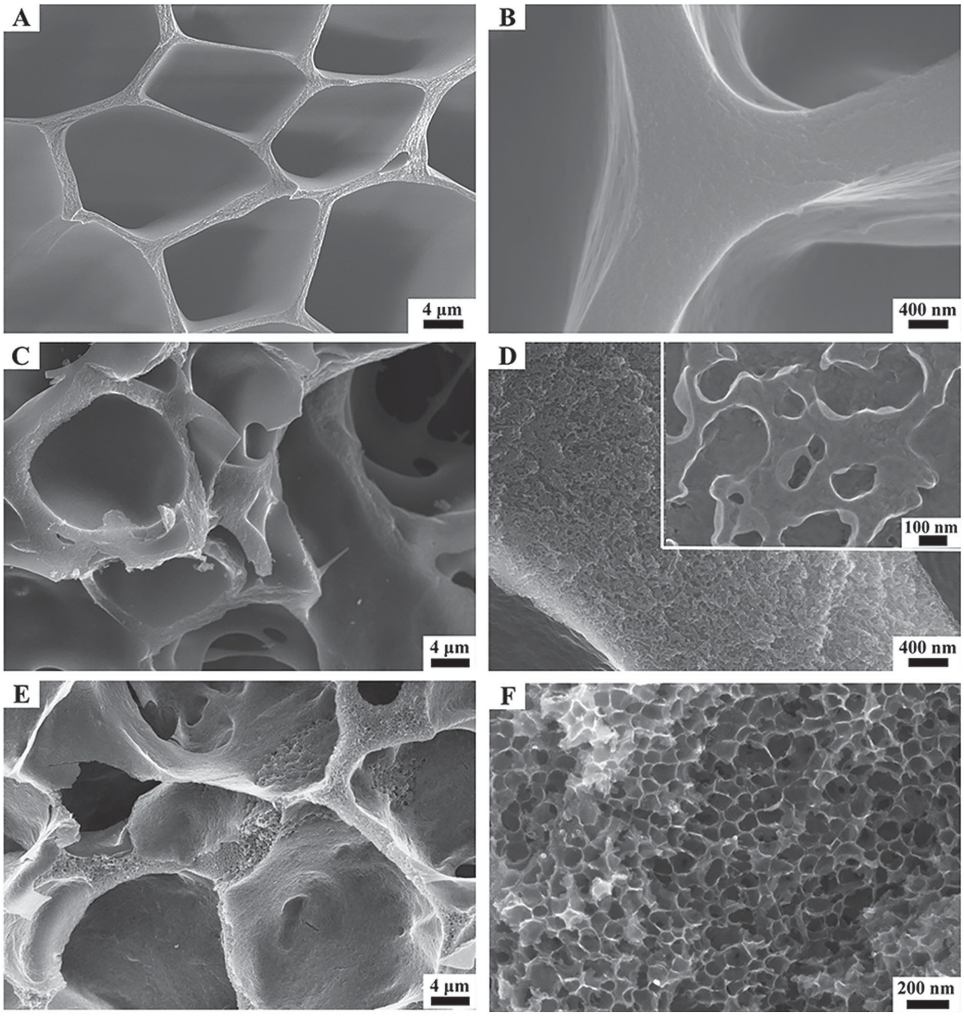

Figure 2. A, B) Field emission scanning electron microscopy (FESEM) images of pure PI based CA, C, D) a-PI based CA, and E, F) a-G-PI based CA at low and high magnifications. Inset in (D) shows FESEM image of a-PI based CA.

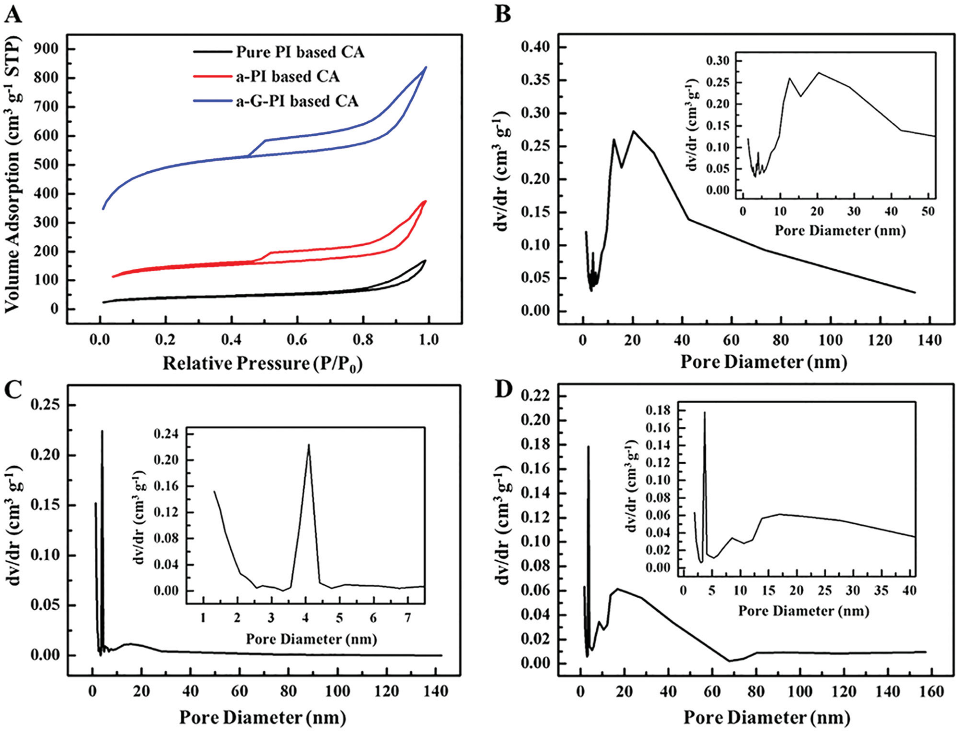

Figure 3. Porosity of three kinds of CAs by N_2 adsorption–desorption analysis. A) N_2 adsorption/desorption isotherm at 77 K. |B) Pore size distribution of pure PI based CA, C) a-PI based CA, and D) a-G-PI based CA as determined by the BJH method.

Nitrogen adsorption/desorption measurements were performed to characterize the specific surface area and porous structure of pure PI based CA, a-PI based CA and a-G-PI based CA, as shown in **Figure 3**. All isotherm curves of these three kinds of CAs belong to type IV with a clear hysteresis loop, suggesting that these CAs possess large quantity of mesopores (Figure 3A). However, the isotherm curve of pure PI based CA and a-PI based CA do not overlap at low relative pressure ($P/P_0 \le 0.45$), while the isotherm curve of a-PI based CA overlaps (Figure S1, Supporting Information). Hence, it can be inferred that the pores in a-G-PI based CA are mostly interconnected while pure PI based CA and a-PI based CA mainly possess closed pores, which is in accordance with SEM observations. The specific surface areas of pure PI based CA, a-PI based CA and a-G-PI based CA are 193.8, 676.5, and 2205.3 m^2 g^{-1}, respectively. It is obvious that the specific surface area of a-G-PI based CA is much larger than those of pure PI based CA and a-PI based CA. In addition, the pore size distribution of pure PI based CA, a-PI based CA, and a-G-PI based CA calculated by the Barrett–Joiner–Halenda (BJH) method are presented in Figure 3B–D. As illustrated in Figure 3B, the pore size of pure PI based CA shows a broad distribution centered at 10–40 nm while a-PI based CA exhibits a relatively narrow pore size distribution centered at 4 nm. However, a-G-PI based CA exhibits hierarchical porous structures with micro-, meso- and macro-pores. As shown in Figure 3D, the pore size distribution of a-G-PI based CA shows a relatively narrow distribution centered at 4 nm and a broad distribution from 15 to 60 nm. Obviously, the microporous structure is derived from the activation of KOH and the mesoporous and the macroporous structure are resulted from the effect of graphene. In this hierarchical system, the micropores will not only increase the specific surface area of CAs, but also facilitate the access of the electrolyte and promote the migration of ions and charges during the process of detection towards DA. Simultaneously, the mesopores and the macropores could offer numerous effective sites for the growth of Fe_2O_3 NPs and control the size of Fe_2O_3 NPs. Thus, the specific surface area and pore size of the obtained PI based CAs can be simply and significantly modulated by KOH activation and the crosslinking of graphene.

The as-prepared a-G-PI based CA NCs with hierarchical porous structures were employed as nano-scaffold for uniform growth of Fe_2O_3 NPs. The loading amount of Fe_2O_3 NPs was carefully tuned by varying the concentration of ferric salt in order to obtain an optimized distribution of Fe_2O_3 NPs, and the morphologies of corresponding nanocomposites were shown in **Figure 4**. As displayed in Figure 4A, Fe_2O_3 NPs are sparsely immobilized on the pore walls of a-G-PI based CAs for Fe_2O_3/a-G-PI based CA-1 due to the low initial ferric salt dosage. With the ferric salt concentration increased to 2×10^{-3} M, Fe_2O_3 NPs are interspersed uniformly on a-G-PI based CAs, both on the surface and inner pore walls, to form Fe_2O_3/a-G-PI based CA-2 (Figure 4B). From the high magnification image of Fe_2O_3/a-G-PI based CA-2, the size of Fe_2O_3 NPs is about 30 nm (Figure 4D). These small and well distributed Fe_2O_3 NPs have more active sites than that of large and aggregated Fe_2O_3 NPs. In sharp contrast, pure Fe_2O_3 NPs prepared by solvothermal reaction without adding a-G-PI based CA consist of large spheres and disorderedly aggregate together (Figure S2, Supporting Information). However, with further increasing

© 2016 WILEY-VCH Verlag GmbH & Co. KGaA, Weinheim

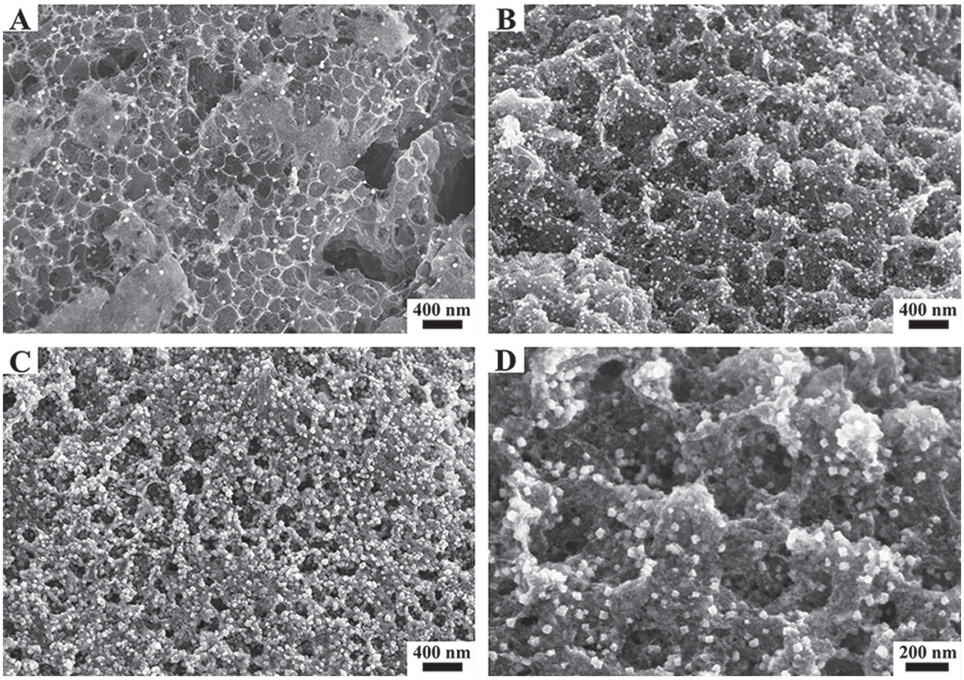

Figure 4. A) FESEM images of Fe_2O_3/a-G-PI based CA-1, B) Fe_2O_3/a-G-PI based CA-2, C) and Fe_2O_3/a-G-PI based CA-5. D) The SEM image of Fe_2O_3/a-G-PI based CA-2 at high magnification.

the concentration of ferric salt, agglomerated Fe_2O_3 NPs with large size can be observed on the pore walls of a-G-PI based CAs (Figure 4C), which will impede the intimate interaction between Fe_2O_3 NPs and a-G-PI based CAs. This phenomenon can be ascribed to the specific growth space for Fe_2O_3 NPs. When the concentration of ferric salt is low, the growth sites are more than Fe_2O_3 seeds. However, when the concentration of ferric salt is too high, the growth sites are less than Fe_2O_3 seeds and all these Fe_2O_3 seeds growing at the same time in the limited space will result in large and aggregated Fe_2O_3 NPs. Therefore, the reasonable amount of a-G-PI based CAs can effectively prevent the aggregation of Fe_2O_3 NPs, maximizing the number of exposed Fe_2O_3 active sites as well as controlling the size of Fe_2O_3 NPs.

The specific surface area and the pore size distribution of pure Fe_2O_3 NPs and Fe_2O_3/a-G-PI based CA-2 are also characterized by N_2 physisorption at 77 K. The specific surface area of Fe_2O_3/a-G-PI based CA-2 is 1141.0 $m^2\ g^{-1}$, which is much larger than that of pure Fe_2O_3 NPs (8 $m^2\ g^{-1}$) as the highly porous a-G-PI based CAs serve as the substrate. Such a high surface area can conduce to the migration of electrolyte, ions and chagers, which will enhance the electrocatalytic performance of DA detection. As illustrated in **Figure 5**A,B, there are almost no pores in Fe_2O_3 NPs, indicating that Fe_2O_3 NPs possess closely packed structure. However, the isotherm curve of Fe_2O_3/a-G-PI based CA-2 overlaps at the low relative pressure ($P/P_0 \leq 0.45$), indicating that the pores in the nanocomposite are mostly interconnected (Figure 5C). In addition, Fe_2O_3/a-G-PI based CA-2 exhibits a relatively narrow pore size distribution centered at 4 nm, suggesting that there are a lot of mesopores in the sample (Figure 5D). Compared with a-G-PI based CA, the pores ranging from 15 to 60 nm disappear in Fe_2O_3/a-G-PI based CA-2 due to the growth and occupation of Fe_2O_3 NPs.

X-ray diffraction (XRD) patterns of the as-prepared a-G-PI based CA, pure Fe_2O_3 NPs, and Fe_2O_3/a-G-PI based CA NCs are shown in **Figure 6**A. The diffraction peaks of a-G-PI based CA are detected at $2\theta = 26°$ (a broad peak) and at $2\theta = 44°$ (a weak peak), which are assigned to the (002) and (100) planes of carbon, respectively. As for pure Fe_2O_3 NPs and Fe_2O_3/a-G-PI based CA NCs, all the diffraction peaks can be indexed to the crystalline hematite phase, which are in good agreement with the literature values (JCPDS: 00-033-0064). As shown in Figure 6A, pure Fe_2O_3 NPs and Fe_2O_3/a-G-PI based CA NCs show sharp peaks at $2\theta = 24.7°$, 33.5°, 35.5°, 41.4°, 49.2°, 54.2°, 61.3°, and 64.3°, which correspond to the (012), (104), (110), (113), (024), (116), (214), and (300) planes of α-Fe_2O_3, respectively. Therefore, the XRD results imply that Fe_2O_3 NPs have been successfully grown on the surface of a-G-PI based CA.

X-ray photoelectron spectroscopy (XPS) measurement is performed to further confirm the the compositions and chemical states of Fe_2O_3/a-G-PI based CA NCs. As shown in Figure 6B, the survey scan indicates that C, Fe, and O elements coexist in Fe_2O_3/a-G-PI based CA NCs, without any detectable impurities. The peak of C 1s spectrum is centered at 284.5 eV, which corresponds to sp[2] C (Figure 6C). The high-resolution Fe 2p spectrum (Figure 6D) exhibits two major peaks with binding energies at 712.5 and 725.3 eV, corresponding to Fe $2p_{3/2}$ and Fe $2p_{1/2}$, respectively, indicating the dominance of Fe (III) in the Fe_2O_3/a-G-PI based CA NC sample. In addition, the shakeup satellite-like peak (characteristic peak) located at 719.2 eV, indicated by arrow in Figure 6D, is characteristic of Fe^{3+} in the obtained NCs. In short, both XRD results and XPS spectrum of Fe 2p confirm the formation of Fe_2O_3. Besides, as calculated

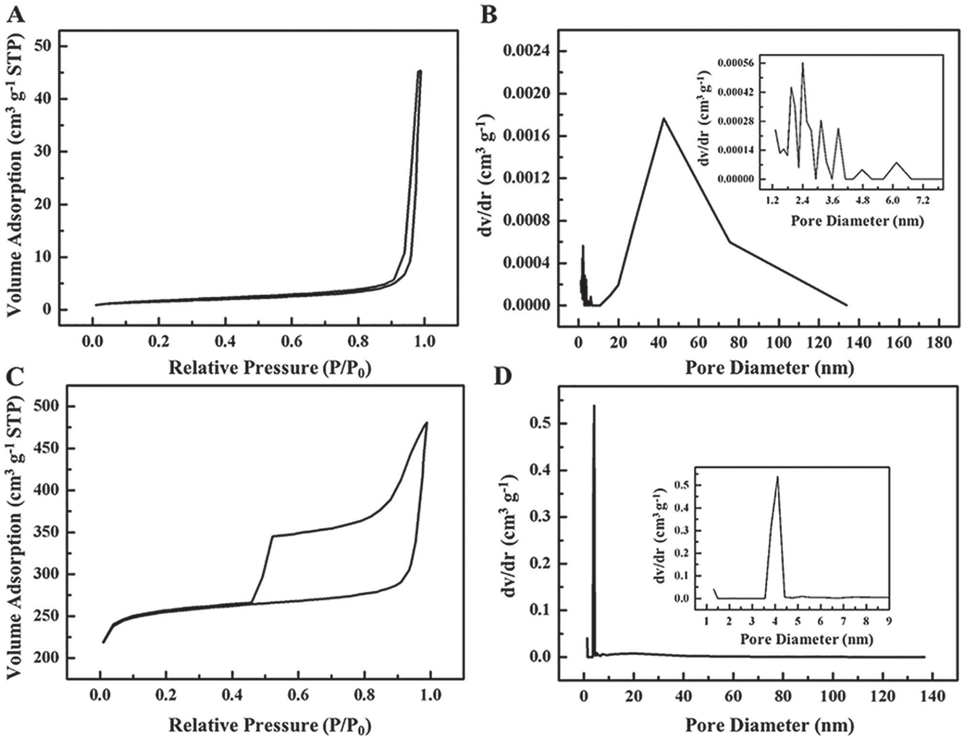

Figure 5. A, B) Porosity of pure Fe_2O_3 and C, D) Fe_2O_3/a-G-PI based CA-2 by N_2 adsorption–desorption analysis. A, C) N_2 adsorption/desorption isotherm at 77 K and B, D) pore size distribution as determined by the BJH method.

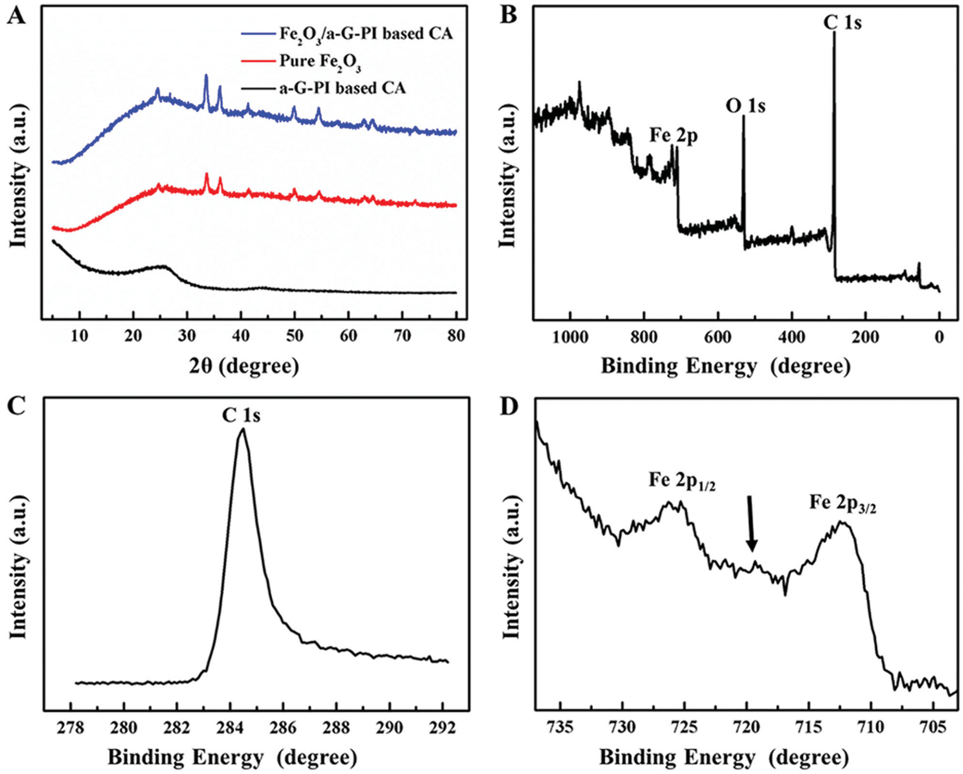

Figure 6. A) XRD patterns of pure Fe_2O_3, a-G-PI based CA and Fe_2O_3/a-G-PI based CA-2. B) XPS survey spectrum, C) C 1s spectrum, and D) Fe 2p spectrum of Fe_2O_3/a-G-PI based CA-2.

© 2016 WILEY-VCH Verlag GmbH & Co. KGaA, Weinheim

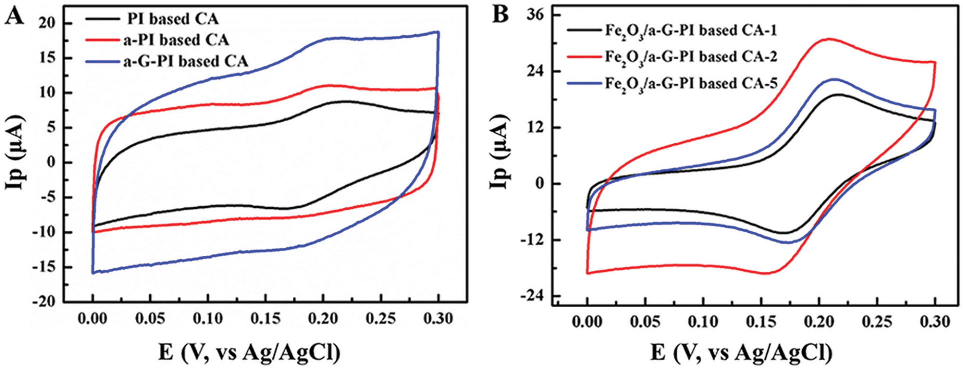

Figure 7. A) Cyclic voltammetry (CV) curves of three kinds of CAs) and B) Fe_2O_3/a-G-PI based CA NGs modified GCE in the presence of 0.1×10^{-3} M DA in pH = 7.0, 0.1 M N_2 saturated PBS (scan rate: 50 mV s^{-1}).

from Figure S3 in the Supporting Information, the content of Fe_2O_3 NPs in the NCs is 8.5, 17.6, and 27.3 wt% for Fe_2O_3/a-G-PI based CA-1, Fe_2O_3/a-G-PI based CA-2 and Fe_2O_3/a-G-PI based CA-5 NCs, respectively.

2.2. Electrochemical Sensing Performance of Fe_2O_3/a-G-PI Based CA NCs

Typically, the dopamine sensors are constructed by direct deposition of the obtained Fe_2O_3/a-G-PI based CA NCs on the surface of bare glassy carbon electrode (GCE). As shown in Figure S4 in the Supporting Information, there are no redox peaks for the a-G-PI based CA, pure Fe_2O_3, and Fe_2O_3/a-G-PI based CA-2 modified GCE in blank PBS solution, suggesting that these samples modified GCE do not have any redox reaction in the selected potential range. For the three kinds of carbon aerogels (pure PI based CA, a-PI based CA, and a-G-PI based CA) modified electrodes, there are remarkable voltammetric response in the presence of DA due to the excellent conductivity, high porosity, and large surface area of the obtained CAs (**Figure 7**A). It is worth noting that the voltammetric response of a-G-PI based CA is the strongest among these CAs, indicating that the electrochemical sensing response for DA detection can be improved by increasing the porosity and the specific surface area. From Figure 7B, it can be easily observed that Fe_2O_3/a-G-PI based CA-2 modified GCE exhibits much larger peak current for the detection of DA than those of the other two Fe_2O_3/a-G-PI based CA NCs (Fe_2O_3/a-G-PI based CA-1 and Fe_2O_3/a-G-PI based CA-5). In contrast, for the pure Fe_2O_3 NPs modified electrode, the peak current is very small due to the aggregation and low specific surface area (Figure S4D, Supporting Information). All these results indicate that the Fe_2O_3/a-G-PI based CA-2 exhibits the optimal electrocatalytic activity for detection of DA. As mentioned above, Fe_2O_3/a-G-PI based CA-2 shows the optimized hierarchical structure with suitable amount and uniform distribution of Fe_2O_3 NPs on the surface of a-G-PI based CA compared with the other two kinds of nanocomposites. In addition, the transport of electrons and ions can be greatly enhanced through the 3D conductive pathways provided by CAs. Thus, in this regard, Fe_2O_3/a-G-PI based CA-2 with proper amount of Fe_2O_3 NPs exhibits the optimized electrocatalytic performance for detection of DA.

To better understand the electrochemical mechanism of the Fe_2O_3/a-G-PI based CA-2 NC sensor for detection of DA, the effect of different scan rates on the CV response is further investigated. As shown in **Figure 8**A, the redox peak current increases gradually with the increase of scan rates. In addition, the response peak current has a good linear relationship with the square root of scan rates from 20 to 350 mV s^{-1}. The linear portions of the response peak current to the square root of different scan rates fit well with the linear regression equation I (μA) = 9.288 $v^{1/2}$ ($mV^{1/2}\ s^{-1/2}$) −34.032 ($R^2 = 0.994$), where I is

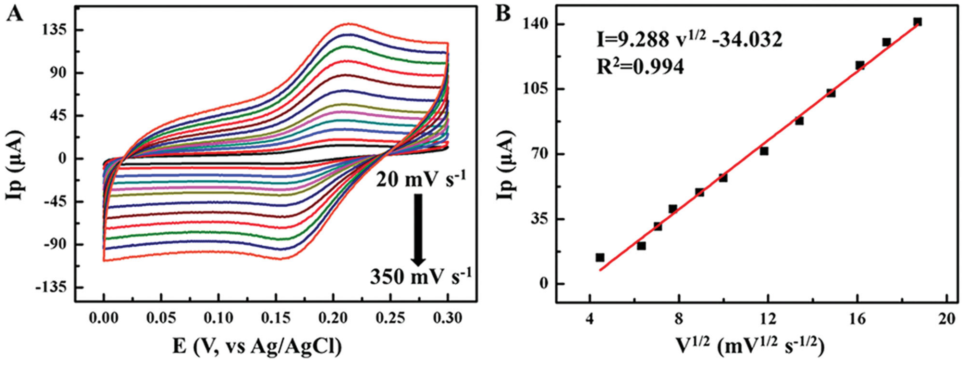

Figure 8. A) CV curves of Fe_2O_3/a-G-PI based CA-2 modified GCE with different scan rates in the presence of 0.1×10^{-3} M DA in pH = 7.0, 0.1 M N_2 saturated PBS. B) The linear relationship of the anodic peak current with the square root of scan rates B).

© 2016 WILEY-VCH Verlag GmbH & Co. KGaA, Weinheim

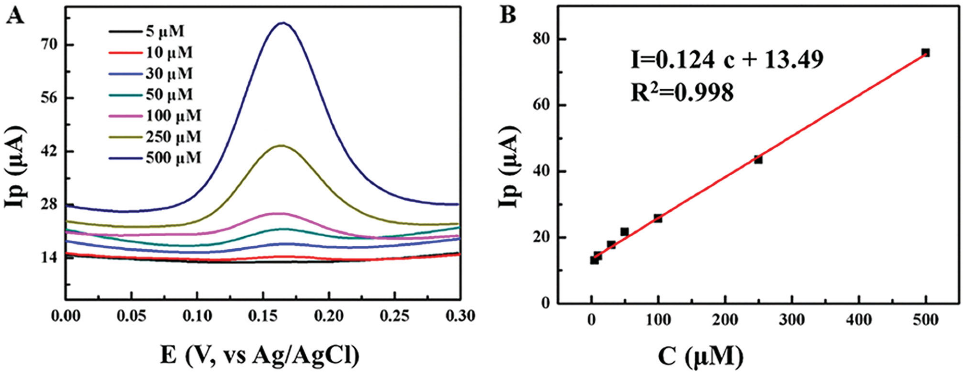

Figure 9. A) DPV curves of different concentrations of DA on Fe_2O_3/a-G-PI based CA-2 in pH = 7.0, 0.1 M N_2 saturated PBS and B) the linear relationship of the anodic peak current with DA concentration.

the peak current, and ν is the scan rate. This result indicates that the redox process of DA is a diffusion-controlled process.

The typical differential pulse voltammetry (DPV) curves of the optimized NC for the oxidation of DA with different DA concentrations in N_2 saturated PBS at the scan rate of 50 mV s^{-1} are shown in **Figure 9**. From Figure 9A, it can be seen that the peak current is greatly enhanced with the increase of DA concentration. Furthermore, the oxidation peak current has a good linear relationship with the DA concentration in the range from 5 to 500 × 10^{-6} M (Figure 9B), indicating that the Fe_2O_3/a-G-PI based CA-2 sensor could be applied for the quantitative detection of DA. From the linear regression equation I (µA) = 0.124 c (×10^{-6} M) + 13.490 (R^2 = 0.998) (where I is the oxidation peak current, and c is the DA concentration), it can be inferred that the detection limit for DA is 0.109 × 10^{-6} M (S/N = 3), which is better than those of ferric oxide based materials and comparable with some noble metal hybrids, as listed in **Table 1**. Therefore, the Fe_2O_3/a-G-PI based CA-2 is a promising candidate for low cost electrocatalysts for detection of DA.

Table 1. Comparison of ferric oxide based materials and some noble metal hybrids modified electrodes for DA detection.

Electrode materials	pH	Detection limit [×10^{-6} M]	Linear range [×10^{-6} M]	Refs.
NiO-CuO/GR	7.4	0.170	0.5–20	[4]
Pt NSs/C_{60}	7.0	0.07	0.5–211.5	[7]
AuNCs/AGR/MWCNT	7.0	0.08 ± 0.02	1.0–210	[8]
PNT-[Cu_4(apyhist)$_4$]4^+/Nafion	7.0	2.800	5.0–40	[11]
Ag-Pt/pCNFs	7.0	0.110	10–500	[17]
Poly(SR)/CPE	7.0	0.700	1.6–16	[22]
EPPGE-SWCNT-Fe_2O_3	7.0	0.360	3–32	[47]
Fe_3O_4-NH_2@GS	7.0	0.126	0.2–38	[60]
Fe_3O_4/rGO/GCE	6.5	0.120	0.5–100	[62]
Pd/rGO	7.0	0.233	1–150	[63]
Fe_2O_3/a-G-PI based CA NCs	7.0	0.109	5–500	This work

GR: graphene; Pt NSs/C_{60}: platinum nanosheets/fullerene; AuNCs: gold nanoclusters; AGR: active graphene; MWCNT: multi-walled carbon nanotubes; PNT: L-diphenylalanine; pCNFs: nanoporous carbon nanofibers; Poly(SR)/CPE: poly(spands reagent)/carbon paste electrode; EPPGEs: edge-plane pyrolytic graphite electrode; SWCNT: single-wall carbon nanotubes; Fe_3O_4-NH_2: amino-group functionalized mesoporous Fe_3O_4; GS: graphene sheets.

The ability to eliminate the interference of the interfering materials commonly coexisting in the target analyte is very important for a biosensor. As we all know, UA and AA always coexist with DA, thus the simultaneous detection of DA in the presence of UA and AA is of great significance. **Figure 10** exhibits the CV curves and DPV curves of 0.1 × 10^{-3} M DA with other interference (0.4 × 10^{-3} M AA and/or 1 × 10^{-3} M UA) on Fe_2O_3/a-G-PI based CA-2 sensor. With UA and/or AA added in the detection solution, no changes of the potential for the oxidation peak of DA can be observed from these two figures, suggesting that the interference of UA and AA can be eliminated effectively during the detection process of DA.

3. Conclusions

In summary, a 3D conductive and highly porous a-G-PI based CA has been successfully fabricated, demonstrating as an excellent template for the growth of well-dispersed Fe_2O_3 NPs. CAs can provide large specific surface area for in situ growth of Fe_2O_3 NPs, effectively preventing the aggregation of Fe_2O_3 NPs and maximizing the number of exposed Fe_2O_3 active sites. The as-obtained Fe_2O_3/a-G-PI based CA NC with the optimal Fe_2O_3 content exhibits enhanced electrochemical sensing performance toward DA with a low detection limit of 0.109 × 10^{-6} M (S/N = 3), a wide linear concentration range from 5 to 500 × 10^{-6} M, and excellent resistance to the interference of UA and AA. The improvement of the NC can be ascribed to the synergistic effect between highly conductive CA and electroactive Fe_2O_3 NPs. Therefore, the highly porous CA supported Fe_2O_3 NPs is a potential candidate as an effective catalyst in electrochemical detection of DA.

4. Experimental Section

Materials: 4,4′-Oxidianiline (ODA), pyromellitic dianhydride (PMDA), triethylamine (TEA, 99%), *N*,*N*-dimethylacetamide (DMAc), 98% H_2SO_4, 30% H_2O_2, $KMnO_4$, 37% HCl, KOH, ferric nitrate nonahydrate, urea, and *N*,*N*-dimethylformamide (DMF) were commercially purchased from Sinopharm Chemical Reagent Co., Ltd. All chemicals were used as received. Natural graphite powder (325 mesh) was purchased from

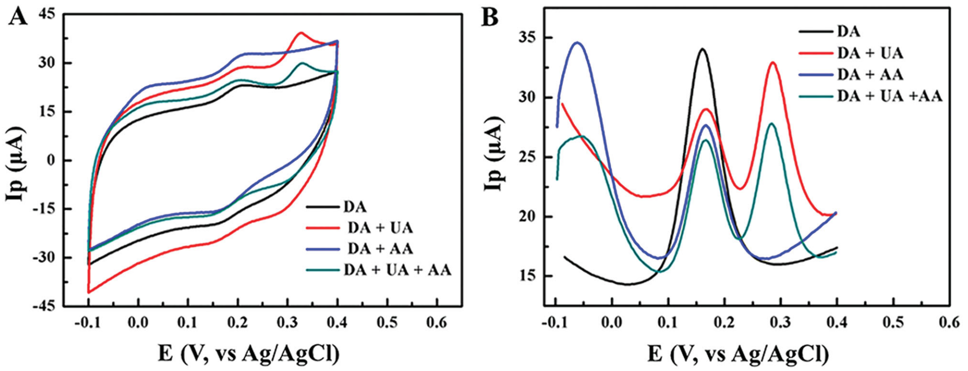

Figure 10. A) CV curves and B) DPV curves of 0.1×10^{-3} M DA with other interference (0.4×10^{-3} M AA and/or 1×10^{-3} M UA) on Fe_2O_3/a-G-PI based CA-2.

Alfa-Aesar (Ward Hill, MA) and used without any other treatments. Deionized (DI) water was used as the solvent throughout the experiments.

Preparation of a-G-PI Based CAs: The precursor of polyimide, water-soluble poly (amic acid) (PAA) oligomer, was prepared according to the method reported previously,[66] and graphene oxide (GO) was prepared from natural graphite according to Hummer's method.[67] The a-G-PI based CAs were synthesized as follows. Briefly, a certain amount of PAA and TEA (weight ratio = 2:1) were dissolved in 8 mg mL^{-1} GO suspension under continuous stirring for 30 min. After PAA was dissolved completely, 1 mL KOH solution (0.5 g mL^{-1}) was quickly poured into the above suspension and kept stirring for 20 min. Then the above suspension was cast into a cylindrical mold followed by gelation at room temperature for at least 12 h to form KOH-GO-PAA hydrogels. Subsequently, the hydrogels were promptly frozen in liquid nitrogen and dried in a lyophilizer for 48 h to form KOH-GO-PAA aerogels. Then, the KOH-GO-PAA aerogels were completely imidized according to the conditions reported previously,[66] and graphene crosslinked polyimide aerogels with KOH were obtained, which was labeled as KOH-G-PI. Finally, the KOH-G-PI aerogels were activated and carbonized subsequently at 450, 750, and 1400 °C for 30, 90, and 60 min, respectively. And, the obtained products were cooled naturally and labeled as a-G-PI based CAs. For comparison, pure PI based CAs and KOH activated PI based carbon aerogels (a-PI based CAs) were also fabricated by the same procedure without the addition of KOH or GO.

Preparation of Fe_2O_3/a-G-PI Based NCs: Fe_2O_3/a-G-PI based CA NCs with various Fe_2O_3 amount were prepared by an in situ solvothermal reaction method. In brief, 404 mg ferric nitrate nonahydrate (1 mmol) and 300 mg urea were added to 60 mL DMF followed by the addition of 50 mg a-G-PI based CAs. After that, the resultant mixtures were transferred to a 100 mL teflon stainless-steel autoclave and reacted at 120 °C for 6 h. After cooling naturally, the obtained composite was collected by a tweezer and subsequently washed with anhydrous ethanol and DI water for several times. The final product was achieved after drying at 80 °C for 6 h and subsequently the composite was annealed at 600 °C for 2 h with a ramping rate of 5 °C min^{-1} under N_2 atmosphere in order to yield crystallized Fe_2O_3/a-G-PI based CA NCs, and the composite was denoted as Fe_2O_3/a-G-PI based CA NCs-1. Additionally, Fe_2O_3/a-G-PI based CA NCs-2 and Fe_2O_3/a-G-PI based CA NCs-5 were prepared by changing the weight of ferric nitrate nonahydrate to 808 and 2020 mg, respectively, by the same procedures. For comparison, Fe_2O_3/a-PI based CA NCs-2 and pure Fe_2O_3 NPs were synthesized under the same conditions.

Characterization: FESEM (Ultra 55, Zeiss) was used to characterize the structure and morphology of the as-prepared a-PI based CAs, a-G-PI based CAs, pure Fe_2O_3 NPs, and Fe_2O_3/a-G-PI based CA NCs at an acceleration voltage of 5 kV. The specific surface area, pore size distribution, and pore volume were characterized with a belsorp-max surface area detecting instrument (Tristar3000) by N_2 physisorption at 77 K. The pore size distributions were derived from the adsorption branches of isotherms using the BJH model. XRD experiments were conducted from $2\theta = 5°$ to $80°$ on an X'Pert Pro X-ray diffractometer with Cu Kα radiation ($\lambda = 0.1542$ nm) under a voltage of 40 kV and a current of 40 mA. The chemical state of Fe, O, and C in the Fe_2O_3/a-G-PI based CA NCs were investigated through the XPS analyses by a VG ESCALAB 220I-XL device. All XPS spectra were corrected using C1s line at 284.5 eV.

Electrochemical Measurements: All electrochemical measurements were performed using a CHI 660D electrochemical workstation (Shanghai Chenhua Instrument Co., China) with a typical three-electrode system (Pt wire as the counter electrode, the samples modified GCE as the working electrode, and Ag/AgCl electrode as the reference electrode). N_2 saturated phosphate buffer solution (0.1 M) was used as an auxiliary electrolyte for the detection of DA. Typically, the samples modified GCE electrode was prepared as follows. 2 mg Fe_2O_3/a-G-PI based CA NCs was dispersed in 1 mL of a mixed solution (DMF and deionized water with a volume ratio of 1:1) by sonicating at least 15 min to form a homogeneous suspension. Finally, the GCE electrode was coated with 8 μL of the above suspension and dried at 70 °C for 30 min. CV and DPV were measured with 0.1×10^{-3} M DA in 0.1 M N_2 saturated PBS solution (pH = 7.0).

Supporting Information

Supporting Information is available from the Wiley Online Library or from the author.

Acknowledgements

The authors are grateful for the financial support from the National Natural Science Foundation of China (51125011, 51433001).

Received: February 18, 2016
Revised: March 7, 2016
Published online: May 6, 2016

---

[1] R. M. Wightman, L. J. May, A. C. Michael, *Anal. Chem.* **1988**, *60*, 769.
[2] F. F. Roussotte, N. Jahanshad, D. P. Hibar, P. M. Thompson, *Brain Imaging Behav.* **2015**, *9*, 213.
[3] A. A. Grace, *Neuropharmacology* **2012**, *62*, 1342.
[4] B. D. Liu, X. Q. Ouyang, Y. P. Ding, L. Q. Luo, D. Xu, Y. Q. Ning, *Talanta* **2016**, *146*, 114.

© 2016 WILEY-VCH Verlag GmbH & Co. KGaA, Weinheim

[5] Y. R. Ma, X. L. Zhang, T. Zeng, D. Cao, Z. Zhou, W. H. Li, H. Y. Niu, Y. Q. Cai, *ACS Appl. Mater. Interfaces* **2013**, *5*, 1024.
[6] Y. J. Han, L. Han, L. L. Zhang, S. J. Dong, *J. Mater. Chem. A* **2015**, *3*, 14669.
[7] X. Zhang, L. X. Ma, Y. C. Zhang, *Electrochim. Acta* **2015**, *177*, 118.
[8] A. A. Abdelwahab, Y. B. Shim, *Sens. Actuators B-Chem.* **2015**, *221*, 659.
[9] J. Zhao, W. M. Zhang, P. Sherrell, J. M. Razal, X. F. Huang, A. I. Minett, J. Chen, *ACS Appl. Mater. Interfaces* **2012**, *4*, 44.
[10] Z. H. Lu, D. M. Chang, J. X. Ma, G. T. Huang, L. K. Cai, L. H. Zhang, *J. Power Sources* **2015**, *275*, 243.
[11] I. D. O. Matos, W. A. Alves, *ACS Appl. Mater. Interfaces* **2011**, *3*, 4437.
[12] X. M. Feng, Y. Zhang, Z. Z. yan, N. N. Chen, Y. W. Ma, X. F. Liu, X. Y. Yang, W. H. Hou, *J. Mater. Chem. A* **2013**, *1*, 9775.
[13] C. Z. Zhu, G. H. Yang, H. Li, D. Du, Y. H. Lin, *Anal. Chem.* **2015**, *87*, 230.
[14] C. Y. Guo, H. H. Huo, X. Han, C. L. Xu, H. L. Li, *Anal. Chem.* **2014**, *86*, 876.
[15] S. Su, J. Chao, D. Pan, L. H. Wang, C. H. Fan, *Electroanalysis* **2015**, *27*, 1062.
[16] C. Zhang, L. H. Qian, K. Zhang, S. L. Yuan, J. W. Xiao, S. Wang, *J. Mater. Chem. A* **2015**, *3*, 10519.
[17] Y. P. Huang, Y. E. Miao, S. S. Ji, W. W. Tjiu, T. X. Liu, *ACS Appl. Mater. Interfaces* **2014**, *6*, 12449.
[18] Y. J. Choi, J. H. Choi, L. C. Liu, B. K. Oh, S. H. Park, *Chem. Mater.* **2013**, *25*, 919.
[19] J. J. Feng, H. Guo, Y. H. Wang, W. Y. Chen, A. J. Wang, *ACS Appl. Mater. Interfaces* **2013**, *5*, 1226.
[20] C. Wang, X. Y. Cheng, X. Zhou, P. Sun, X. L. Hu, K. G. Shimanoe, G. Y. Lu, N. Yamazoe, *ACS Appl. Mater. Interfaces* **2014**, *6*, 12031.
[21] L. Wang, X. P. Lu, C. J. Wen, Y. Z. Xie, L. F. Miao, S. H. Chen, H. B. Li, P. Li, Y. H. Song, *J. Mater. Chem. A* **2015**, *3*, 608.
[22] Y. V. M. Reddy, P. V. Rao, A. V. B. Reddy, M. Lavanya, M. Venu, G. Madhavi, *Mater. Sci. Eng. C* **2015**, *57*, 378.
[23] V. Urbanova, M. Magro, A. Gedanken, D. Baratella, *Chem. Mater.* **2014**, *26*, 6653.
[24] M. L. Liu, Q. Chen, C. L. Lai, Y. Y. Zhang, J. H. Deng, H. T. Li, S. Z. Yao, *Biosens. Bioelectron.* **2013**, *48*, 75.
[25] Y. X. Liu, W. J. Zhu, D. Wu, Q. Wei, *Measurement* **2015**, *60*, 1.
[26] H. Teymourian, A. Salimi, S. Khezrian, *Biosens. Bioelectron.* **2013**, *49*, 1.
[27] J. H. Ke, Z. K. Wang, Y. Z. Li, Q. L. Hu, J. Feng, *Chin. J. Polym. Sci.* **2012**, *30*, 436.
[28] Z. Y. Wang, Y. Y. Bai, W. C. Wei, N. Xia, Y. H. Du, *Materials* **2013**, *6*, 5690.
[29] J. Chen, L. Xu, W. Y. Li, *Adv. Mater.* **2005**, *17*, 582.
[30] F. Bao, J. L. Yao, R. A. Gu, *Langmuir* **2009**, *25*, 10782.
[31] X. L. Hu, J. C. Yu, J. M. Gong, Q. Li, G. H. Li, *Adv. Mater.* **2007**, *19*, 2324.
[32] X. Cao, N. Wang, *Analyst* **2011**, *136*, 4241.
[33] C. Lu, X. J. Liu, Y. F. Li, F. Yu, L. H. Tang, Y. J. Hu, Y. B. Ying, *ACS Appl. Mater. Interfaces* **2015**, *7*, 15395.
[34] Q. Y. Liu, L. Y. Zhang, H. Li, Q. Y. Jia, Y. L. Jiang, Y. T. Yang, R. R. Zhu, *Mater. Sci. Eng. C* **2015**, *55*, 193.
[35] R. Suresh, K. Giribabu, R. Manigandan, A. Stephen, V. Narayanan, *RSC Adv.* **2014**, *4*, 17146.
[36] Z. Y. Yu, H. J. Li, J. H. Lu, X. M. Zhang, N. K. Liu, X. Zhang, *Electrochim. Acta* **2015**, *158*, 264.
[37] B. Šljuki , C. E. Banks, R. G. Compton, *Nano Lett.* **2006**, *6*, 1556.
[38] J. P. Wang, H. Gao, F. L. Sun, Q. Hao, C. X. Xu, *Biosens. Bioelectron.* **2013**, *42*, 550.
[39] M. M. Y. Wang, T. Shen, M. Wang, D. E. Zhang, Z. W. Tong, J. Chen, *Sens. Actuators B* **2014**, *190*, 645.
[40] Z. Zhang, X. Wang, X. A. Yang, *Analyst* **2011**, *136*, 4960.
[41] L. L. Wang, Z. Lou, J. N. Deng, R. Zhang, T. Zhang, *ACS Appl. Mater. Interfaces* **2015**, *7*, 13098.
[42] Y. Wang, J. L. Cao, S. R. Wang, X. Z. Guo, J. Zhang, H. J. Xia, S. M. Zhang, S. H. Wu, *J. Phys. Chem. C* **2008**, *112*, 17804.
[43] L. L. Wang, T. Fei, Z. Lou, T. Zhang, *ACS Appl. Mater. Interfaces* **2011**, *3*, 4689.
[44] T. L. Xu, N. K. Scafa, L. P. Xu, L. Su, C. Z. Li, S. F. Zhou, Y. Liu, X. J. Zhang, *Electroanalysis* **2014**, *26*, 449.
[45] Z. Y. Sun, H. Q. Yuan, Z. M. Liu, B. X. Han, X. R. Zhang, *Adv. Mater.* **2005**, *17*, 2993.
[46] S. Radhakrishnan, K. Krishnamoorthy, C. Sekar, J. Wilson, S. J. Kim, *Appl. Catal. B* **2014**, *148–149*, 22.
[47] A. S. Adekunle, *Sens. Actuators B* **2010**, *148*, 93.
[48] H. Shan, C. B. Liu, J. B. Zhang, H. Y. Li, Z. Liu, X. B. Zhang, X. Q. Bo, X. Chi, *ACS Appl. Mater. Interfaces* **2013**, *5*, 6376.
[49] S. Jana, A. Mondal, *ACS Appl. Mater. Interfaces* **2014**, *6*, 15832.
[50] P. Sun, C. Wang, J. Y. Liu, X. Zhou, X. W. Li, X. L. Hu, G. Y. Lu, *ACS Appl. Mater. Interfaces* **2015**, *7*, 19119.
[51] M. T. Niu, F. Huang, L. F. Cui, P. Huang, Y. L. Yu, Y. S. Wang, *ACS Nano* **2010**, *4*, 681.
[52] M. S. Hsu, Y. L. Chen, C. Y. Lee, H. T. Chiu, *ACS Appl. Mater. Interfaces* **2012**, *4*, 5570.
[53] L. Wang, H. R. Xu, Y. L. Song, J. P. Luo, W. J. Wei, S. W. Xu, X. X. Cai, *ACS Appl. Mater. Interfaces* **2015**, *7*, 7619.
[54] G. Fabregat, E. Armelin, C. Alemán, *J. Phys. Chem. B* **2014**, *118*, 4669.
[55] L. S. Lin, Z. X. Cong, J. B. Cao, K. M. Ke, Q. L. Peng, J. H. Cao, H. H. Yang, G. Liu, X. Y. Chen, *ACS Nano* **2014**, *8*, 3876.
[56] D. B. Lu, Y. Zhang, L. T. Wang, S. X. Lin, C. M. Wang, X. F. Chen, *Talanta* **2012**, *88*, 181.
[57] Y. Jie, N. Wang, X. Cao, Y. Xu, T. Li, X. J. Zhang, Z. L. Wang, *ACS Nano* **2015**, *9*, 8376.
[58] M. Zhang, C. Z. Liao, Y. L. Yao, Z. K. Liu, F. F. Gong, T. Yan, *Adv. Funct. Mater.* **2014**, *24*, 978.
[59] M. Khan, M. N. Tahir, S. F. Adil, H. U. Khan, M. H. Siddiqui, A. A. Al-warthan, W. Tremel, *J. Mater. Chem. A* **2015**, *3*, 18753.
[60] D. Wu, Y. Y. Li, Y. Zhang, P. P. Wang, Q. Wei, B. Du, *Electrochim. Acta* **2014**, *116*, 244.
[61] M. M. Shahid, P. Rameshkumar, A. Pandikumar, H. N. Lim, Y. H. Ng, N. M. Huang, *J. Mater. Chem. A* **2015**, *3*, 14458.
[62] P. S. Teo, P. Alagarsamy, N. M. Huang, H. N. Lim, S. Yusran, *Sensors* **2014**, *14*, 15227.
[63] S. Palanisamy, S. Ku, S. M. Chen, *Microchim. Acta* **2013**, *180*, 1037.
[64] J. Samseya, R. Srinivasan, A. Daniel Arulraj, V. S. Vasantha, *Electroanalysis* **2014**, *26*, 1702.
[65] L. A. Mercante, A. Pavinato, L. E. O. Iwaki, V. P. Scagion, V. Zucolotto, O. N. Oliverira, L. H. C. Mattoso, D. S. Correa, *ACS Appl. Mater. Interfaces* **2015**, *7*, 4784.
[66] Y. F. Zhang, W. Fan, Y. P. Huang, C. Zhang, T. X. Liu, *RSC Adv.* **2015**, *5*, 1301.
[67] W. S. Hummers, R. E. Offeman, *J. Am. Chem. Soc.* **1958**, *80*, 1339.
[68] J. C. Wang, S. Kaskel, *J. Mater. Chem.* **2012**, *22*, 2370.

© 2016 WILEY-VCH Verlag GmbH & Co. KGaA, Weinheim